Tunable Optical Properties and Charge Separation in CH$_3$NH$_3$Sn$_x$Pb$_{1−x}$I$_3$/TiO$_2$-Based Planar Perovskites Cells

Hong-Jian Feng,*[†,‡] Tula R. Paudel,[‡] Evgeny Y. Tsymbal,[‡] and Xiao Cheng Zeng*[§]

[†]School of Physics, State Key Lab Incubation Base of Photoelectric Technology and Functional Materials, and International Collaborative Center on Photoelectric Technology and Nano Functional Materials, Northwest University, Xi'an 710069, People's Republic of China

[‡]Department of Physics and Astronomy and [§]Department of Chemistry, University of Nebraska-Lincoln, Lincoln, Nebraska 68588, United States

S *Supporting Information*

ABSTRACT: A sharp potential drop across the interface of the Pb-rich halide perovskites/TiO$_2$ heterostructure is predicted from first-principles calculations, suggesting enhanced separation of photoinduced charge carriers in the perovskite-based photovoltaic solar cells. The potential drop appears to be associated with the charge accumulation at the polar interface. More importantly, on account of both the β phase structure of CH$_3$NH$_3$Sn$_x$Pb$_{1−x}$I$_3$ for $x < 0.5$ and the α phase structure of CH$_3$NH$_3$Sn$_x$Pb$_{1−x}$I$_3$ for $x \geq 0.5$, the computed optical absorption spectra from time-dependent density functional theory (TD-DFT) are in very good agreement with the measured spectra from previous experiments. Our TD-DFT computation also confirms the experimental structures of the mixed Pb-Sn organometal halide perovskites.

These computation results provide a highly sought answer to the question why the lead-based halide perovskites possess much higher power conversion efficiencies than the tin-based counterparts for solar-cell applications.
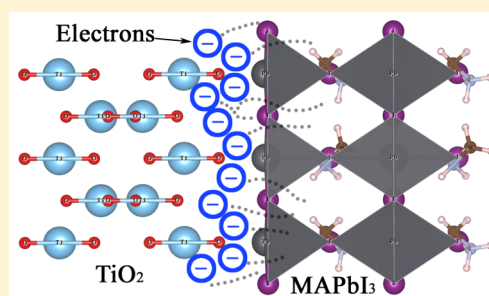
1. INTRODUCTION

The third-generation hybrid halide perovskites, i.e., MAPbX$_3$ (MA = CH$_3$NH$_3^+$, X = Cl, Br, I) based solar cells have been under very fast development over the past three years with the power conversion efficiency (PCE) rapidly improved from 3.8%[1] to a certified value of 20.1%.[2] Recently, Y:TiO$_2$(yttrium-doped TiO$_2$)/MAPbI$_{3−x}$Cl$_x$/spiro-MeOTAD(2,2′,7,7′-tetrakis (N,N-di-p-methox- yphenylamine)-9,9′-spirobifluorene) has reached the PCE of 19.3% (the highest PCE reported in the literature) as well as an open circuit voltage (V_{oc}) of 1.13 V.[3] However, lead is toxic to humans and organisms. This limits potentially wide application of MAPbI$_3$-based solar cells. On the other hand, MASnI$_3$-based heterostructures[4,5] have been suggested as an alternative to replace the lead perovskites. However, MASnI$_3$ still has relatively low PCE (6.3%) and V_{oc} (0.57 V). More effort is needed to achieve lead-free solid-state solar cells with high PCE and low cost. Recently, several groups have reported different solution-processing methods to prepare mixed Sn and Pb perovskites MASn$_x$Pb$_{1−x}$I$_3$ for which tunable band gap and high carrier mobilities can be achieved.[6−8] Notably, Ogomi et al. observed a linear decrease of band gap with increasing the Sn content,[7] whereas Hao et al. found a nonlinear relationship between the band gap and the Sn content.[8] Stoumpos et al. show that samples prepared from different solution-processing methods can give rise to very different optical performance, resulting in different relationships between the Pb/Sn ratio and band gap.[6] MASn$_x$Pb$_{1−x}$I$_3$ is known to be the tetragonal p4mm phase, i.e., the α phase, for $x \geq 0.5$, but is in the tetragonal I4cm phase, i.e., the β phase,

for $x < 0.5$. Hence, it appears to us that two major factors that can influence the band gap: the crystalline structure of the bulk crystal and the Pb/Sn ratio. It is important to know which factor is more dominant to the optical absorption and band gap.

Several theoretical studies of the electronic and optical properties of organohalide lead perovskites using density functional theory (DFT) methods have been reported.[9−13] It has been shown that by considering the spin−orbit coupling (SOC) effect of the heavy elements Pb and I, the degeneracy of the bands near the conduction band minimum (CBM) and valence band maximum (VBM) can be removed, and the band gap can be reduced by 1 eV.[14−16] It turns out that the electronic properties including the band characters can be properly described without considering the SOC effect.[17] Although the hybrid DFT methods such as HSE06[12,18] or the GW approximation[19,20] can give more accurate electronic structures and absorption energies, the computing task will be highly demanding due to the large system considered (over 100 atoms). In this study, we will use time-dependent DFT (TD-DFT)[21,22] to compute optical properties of the perovskite systems. Previous studies have shown that optical properties computed from TD-DFT are in agreement with experiment. Moreover, the response charge density from TD-DFT can be related to the photoinduced carrier transport in the excited states. We note that SOC-GW method has been utilized very recently to study the mixed Pb-Sn
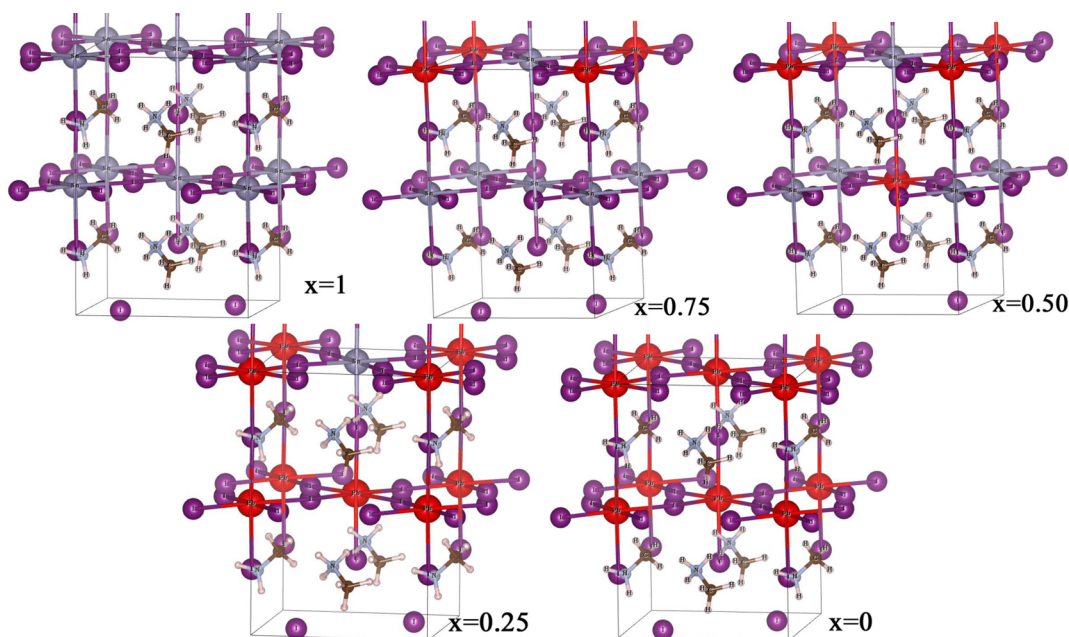
Figure 1. Crystal structures for β-CH$_3$NH$_3$Sn$_x$Pb$_{1-x}$I$_3$ with x corresponding to 1, 0.75, 0.50, 0.25, and 0, respectively. The gray and red balls indicate the Sn and Pb atoms, respectively.

compounds, which results in a linear relationship between the Pb/Sn ratio and the band gap.[23] However, only the tetragonal *I4cm* symmetry, i.e., β phase structure, was considered in that study. As mentioned above, both crystalline structures of the bulk crystal and the Pb/Sn ratio can influence the optical behavior and bandgap tunability and thus should be considered. In addition, the photoinduced carrier transport needs to be investigated as well. By taking into account both the α and β phases, we have performed systematic TD-DFT and DFT computations to determine structures of the Pb-Sn mixed halide perovskites and to compare with latest experimental results. To our knowledge, TD-DFT investigation of the optical properties of the Pb-Sn mixed halide perovskites has not been reported in the literature.

Note also that in realistic solar-cell experiments, the electron transport material (ETM), e.g., TiO$_2$, and the organic hole transport material (HTM), e.g., spiro-MeOTAD, are often incorporated with halide perovskites to achieve separation of photoinduced carriers.[24−29] However, the organic HTM can be easily decomposed in the solution. This also limits long-term stability of the perovskite-based solar cells. Many studies have been devoted to the HTM-free solar cells. For example, planar MAPbI$_3$/TiO$_2$ and mixed-cation perovskite (5-AVA)$_x$(MA)$_{1-x}$PbI$_3$/TiO$_2$ heterostructure solar cells appear to be promising candidates as HTM-free perovskite-based photovoltaic cells.[30,31] In this case, the halide perovskites act as the p-type doped p−i−n junction where the hole and electron can be separated, while TiO$_2$ performs like an ETM. Moreover, TiO$_2$ plays a role for the enhancement of photovoltaic performance in the TiO$_2$-based heterostructures through the interfacial interactions.[32,33] The carrier transport in the interface of the MASn$_x$Pb$_{1-x}$I$_3$/TiO$_2$ heterojunction-based solar cells, however, is still unclear. So we have also performed DFT computations to investigate the carrier transport mechanism underlying the Pb-Sn perovskite-based heterostructures.

2. COMPUTATIONAL METHODS

Quantum ESPRESSO code has been utilized to perform the DFT and TD-DFT computations.[34] The Perdew−Burke−Ernzerhof (PBE)

parametrization of the generalized gradient approximation improved for a solid (PBEsol) is adopted to describe the exchange−correlation interactions.[35] Projector augmented-wave (PAW) pseudopotentials are used to evaluate the valence states and the interactions between valence electrons and ions.[36,37] The 192-atom $2\sqrt{2} \times 2\sqrt{2} \times 2$ CH$_3$NH$_3$Sn$_x$Pb$_{1-x}$I$_3$ supercells are used to compute the optical spectra, and the 48-atom $\sqrt{2} \times \sqrt{2} \times 2$ CH$_3$NH$_3$Sn$_x$Pb$_{1-x}$I$_3$ supercells are used to compute the electronic properties. For CH$_3$NH$_3$Sn$_x$Pb$_{1-x}$I$_3$/TiO$_2$ heterostructures, we use a slab model with a thickness about 25 Å. The vacuum layer thickness is the same as the atomic layer. The $8 \times 8 \times 8$ and $8 \times 8 \times 1$ Monkhorst−Pack sampling of the Brillouin zone are used to ensure the convergence in the total energy calculations of the bulk and slab structures, respectively. Several TiO$_2$ terminations are at the interface with CH$_3$NH$_3$Sn$_x$Pb$_{1-x}$I$_3$. However, it is experimentally shown that the {0 0 1} facets of TiO$_2$ are beneficial for the photovoltaic applications,[30,31] and therefore in this study, we focus only on the (0 0 1) interface. Even with this alignment, there are two possible interface terminations: Pb(Sn)I$_2$/TiO$_2$ and CH$_3$NH$_3$I/TiO$_2$. We found that CH$_3$NH$_3$I/TiO$_2$ interface is unstable and therefore considered only Pb(Sn)I$_2$/TiO$_2$ interface. We have optimized the atomic structure of this interface assuming that the TiO$_2$ is stoichiometric. The lattice parameters for the TiO$_2$, mixed perovskites, and the corresponding heterostructures are given in Table 1. The geometry structures for CH$_3$NH$_3$Sn$_x$Pb$_{1-x}$I$_3$/TiO$_2$ are fully optimized for $x = 0$, 0.5, and 1 without any symmetry constraints, and the lattice constants for CH$_3$NH$_3$Sn$_x$Pb$_{1-x}$I$_3$ are taken from the experimental values[7] with atomic positions optimized, for which the forces on the ions are <0.001 Ry/au. For all the slab calculations, the bottom layer of the TiO$_2$ is fixed to mimic the compact TiO$_2$ scaffold in the planar heterojunction solar cells. Ferroelectric polarization (**P**) is calculated within the modern theory of polarization.[38,39] The polarization is considered as the sum of two parts:

$$\mathbf{P}_{mac} = \mathbf{P}_{ion} + \mathbf{P}_{el} \tag{1}$$

Here the electronic contribution is given by[38,39]

$$\mathbf{P}_{el} = -\frac{ef}{(2\pi)^3} \int_{BZ} dk \langle u_{nk} | i\nabla_k | u_{nk} \rangle \tag{2}$$

where f is the spin degeneracy, u_{nk} is the cell-periodic functions, and e is the electron charge. The electronic contribution projected to the reciprocal lattice vector, $\mathbf{b}_i$, is given by[38,39]

$$\mathbf{P}_{el} \cdot \mathbf{b}_i = \frac{fe}{\Omega N_\perp^i} \sum_{l=1}^{N_\perp^i} \operatorname{Im} \ln \prod_{j=0}^{N_i - 1} \det S(\mathbf{k}_j^{(i)}, \mathbf{k}_{j+1}^{(i)}) \tag{3}$$

where $N_\perp^l = N_2 \times N_3$ is the number of divisions along $\mathbf{b}_1$. N_2 and N_3 are the number of divisions along $\mathbf{b}_2$ and $\mathbf{b}_3$, respectively. Seven divisions in the perpendicular $\mathbf{k}$ direction are used in the calculation of $\mathbf{P}_{el}$. S is the overlap integral in the k-space and is given by

$$S_{nm}(\mathbf{k}, \mathbf{k}') = \langle u_{nk} | u_{mk'} \rangle \tag{4}$$

where n and m run over the occupied bands.

3. RESULTS AND DISCUSSION

3.1. Structures of $CH_3NH_3Sn_xPb_{1-x}I_3$ and the Heterostructures.

The crystal structures of the mixed Pb-Sn halide perovskites in β phase are shown in Figure 1. For $CH_3NH_3Sn_{0.50}Pb_{0.50}I_3$ in a 48-atom supercell, there are three

configurations which are not equivalent, and only the diagonal structure is shown in Figure 1. In 192-atom supercells, there are 11 inequivalent configurations for $CH_3NH_3Sn_{0.50}Pb_{0.50}I_3$ and 8 inequivalent configurations for $CH_3NH_3Sn_{0.25}Pb_{0.75}I_3$. The different configurations give no significant difference in the

Table 1. Lattice Constants of the TiO$_2$, Mixed Pb-Sn compounds, and Heterostructures Used in Our Calculations[a]

	a (Å)	b (Å)	c (Å)	$\alpha = \beta = \gamma$ (deg)
α-$CH_3NH_3SnI_3$ (exp.)	6.240	6.240	6.281	90
α-$CH_3NH_3Sn_{0.75}Pb_{0.25}I_3$ (exp.)	6.283	6.283	6.314	90
α-$CH_3NH_3Sn_{0.50}Pb_{0.50}I_3$ (exp.)	6.348	6.348	6.379	90
α-$CH_3NH_3Sn_{0.25}Pb_{0.75}I_3$ (exp.)	6.315	6.315	6.300	90
α-$CH_3NH_3PbI_3$ (exp.)	6.315	6.315	6.244	90
β-$CH_3NH_3SnI_3$ (exp.)	8.823	8.823	12.562	90
β-$CH_3NH_3Sn_{0.75}Pb_{0.25}I_3$ (exp.)	8.884	8.884	12.628	90
β-$CH_3NH_3Sn_{0.50}Pb_{0.50}I_3$ (exp.)	8.976	8.976	12.758	90
β-$CH_3NH_3Sn_{0.25}Pb_{0.75}I_3$ (exp.)	8.930	8.930	12.599	90
β-$CH_3NH_3PbI_3$ (exp.)	8.929	8.929	12.688	90
TiO$_2$ (opt.)	3.923	3.923	9.846	90
β-$CH_3NH_3PbI_3$/TiO$_2$ (opt.)	8.323	8.323	56.464	90

	a′ (Å)	b′ (Å)	c′ (Å)	$\alpha = \beta = \gamma$ (deg)
α-$CH_3NH_3SnI_3$ (exp.)	8.823	8.823	12.562	90
α-$CH_3NH_3SnI_3$/TiO$_2$ (opt.)	8.187	8.187	45.718	90
α-$CH_3NH_3Sn_{0.50}Pb_{0.50}I_3$/TiO$_2$ (opt.)	8.308	8.308	45.718	90

[a]Exp. and opt. indicate the structures taken from the experiments and the fully optimized structures, respectively. $a\sqrt{2} \times b\sqrt{2} \times c2$ supercell of α-$CH_3NH_3SnI_3$ and $a2 \times b2 \times c$ supercell of TiO$_2$ are used to build the corresponding heterostructures.
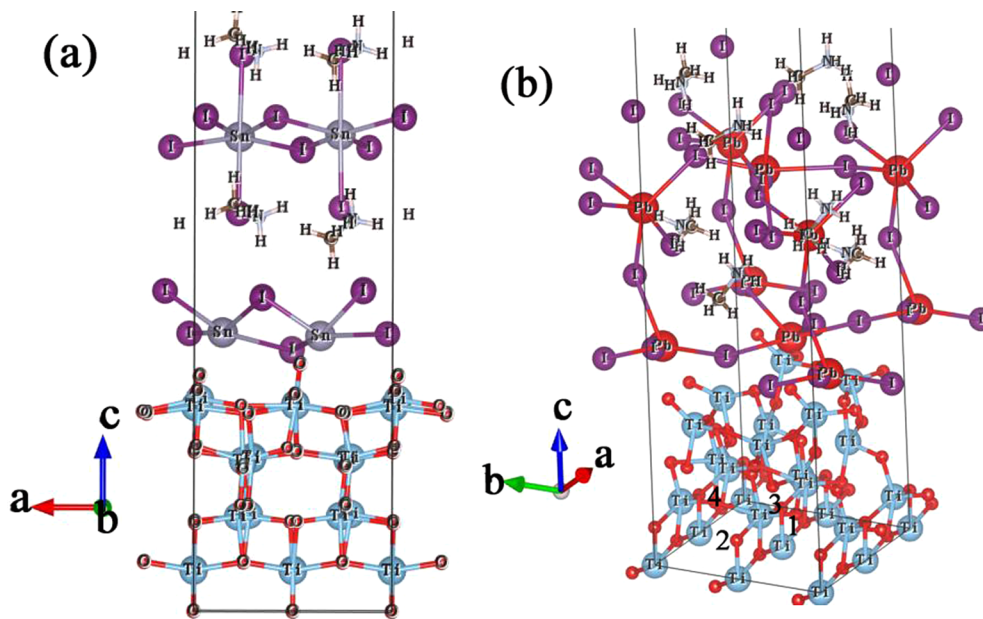

Figure 2. Top view from c axis for α and β phase halide perovskites, respectively.

Figure 3. Optimized structures for (a) α-$CH_3NH_3SnI_3$/TiO$_2$ and (b) β-$CH_3NH_3PbI_3$/TiO$_2$, respectively. As can be seen from Table 1, the α-$CH_3NH_3SnI_3$ part is under about −7% compressive strain (i.e., from 8.823 Å to 8.187 Å), while the TiO$_2$ part is under about 4% expansion strain (i.e., from 7.846 Å to 8.187 Å). The β-$CH_3NH_3PbI_3$ part is under about -6% compressive strain (i.e., from 8.929 Å to 8.323 Å), while the TiO$_2$ part is under about 6% expansion strain (i.e., from 7.846 Å to 8.323 Å). The gray and red balls denote the Sn and Pb atoms, respectively.

Table 2. Bond Lengths of α-MASnI$_3$, β-MAPbI$_3$, TiO$_2$, α-MASnI$_3$/TiO$_2$, and β-MAPbI$_3$/TiO$_2$ after Geometry Optimization[a]

bond length (Å)	α-MASnI$_3$	β-MAPbI$_3$	TiO$_2$	α-MASnI$_3$/TiO$_2$	β-MAPbI$_3$/TiO$_2$
Pb(Sn)-I$_a$1	3.235	3.251	–	3.383	3.244
Pb(Sn)-I$_a$2	3.074	3.275	–	3.158	3.253
Pb(Sn)-I$_e$1	3.256	3.137	–	3.098	2.965
Pb(Sn)-I$_e$2	3.136	3.147	–	3.080	3.120
Pb(Sn)-I$_e$3	3.059	3.173	–	3.234	3.594
Pb(Sn)-I$_e$4	3.156	3.182	–	3.021	2.970
Ti-O$_a$1	–	–	1.976	1.993	1.947
Ti-O$_a$2	–	–	1.976	1.940	1.890
Ti-O$_e$1	–	–	1.933	1.807	1.836
Ti-O$_e$2	–	–	1.933	1.875	2.037
Ti-O$_e$3	–	–	1.933	2.268	2.229
Ti-O$_e$4	–	–	1.933	2.485	2.288

[a]The apical and equatorial sites of the iodine ions in a Pb(Sn)-I$_6$ cage are indicated by I$_a$ and I$_e$, respectively. The locations of O$_a$ and O$_e$ are site dependent. The apical and equatorial sites of the O in Ti-O$_6$ cage are indicated by O$_a$ and O$_e$, respectively.
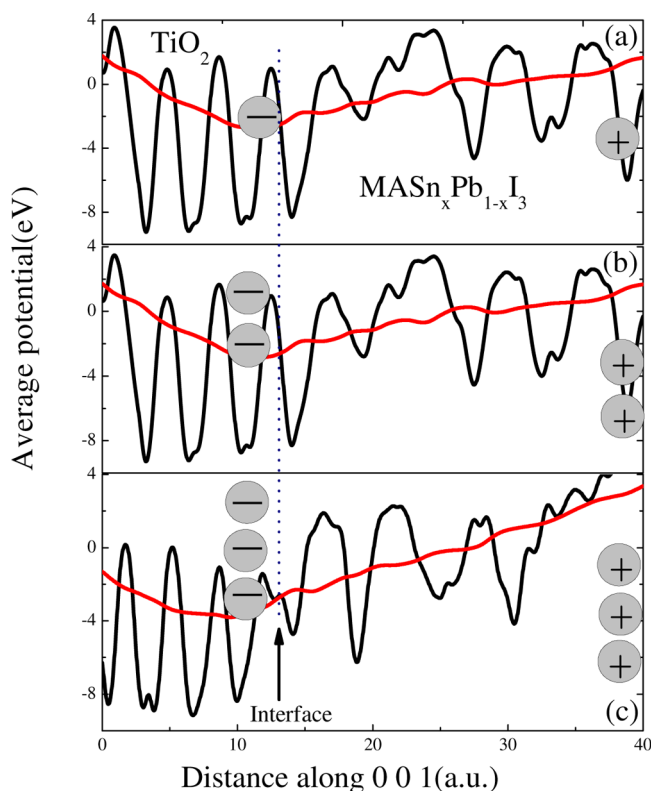

Figure 4. Plane-averaged electrostatic potentials along [0 0 1] direction for (a) CH$_3$NH$_3$SnI$_3$/TiO$_2$, (b) CH$_3$NH$_3$Sn$_{0.50}$Pb$_{0.50}$I$_3$/TiO$_2$, and (c) CH$_3$NH$_3$PbI$_3$/TiO$_2$ heterostructures, respectively. The black and red lines indicate the microscopic and macroscopic averaged-potentials, respectively.

electronic characters. Therefore, we only used the structures shown in Figure 1. Pb(Sn)−I−Pb(Sn) angle in ab plane of Pb-rich phase, i.e., β phase with $I4cm$ symmetry, is deviated from the straight angle slightly bigger than in Sn-rich phase, i.e., α phase with $P4mm$ symmetry, leading to the lower symmetry. The top view from c axis for α-MASnI$_3$ and β-MAPbI$_3$ is shown in Figure 2. The unit cells of the two crystalline structures can be connected by a $a\sqrt{2} \times b\sqrt{2} \times c2$ relation, and the unit-cell

volume in β phase is increased by 4-fold. Keeping in mind the difference in the structures and symmetry of the two phases, we just provide the crystal structures of the β phase with varying Pb/Sn ratio, and the α phase structures can be obtained easily.

The optimized heterogeneous structures of α-CH$_3$NH$_3$SnI$_3$/TiO$_2$ and β-CH$_3$NH$_3$PbI$_3$/TiO$_2$ are shown in Figure 3. We use the $a\sqrt{2} \times b\sqrt{2} \times c2$ supercell of the α-CH$_3$NH$_3$SnI$_3$ and the $a2 \times b2 \times c$ supercell of TiO$_2$ to build the corresponding heterostructures. The Pb(Sn)−I and Ti−O bond lengths in the mixed Pb-Sn compounds and the heterostructures are given in Table 2. SnI$_2$ layers in α-CH$_3$NH$_3$SnI$_3$/TiO$_2$ moves toward the TiO$_2$ side, much closer than the PbI$_2$ layers in β-CH$_3$NH$_3$PbI$_3$/TiO$_2$. The Pb(Sn)I$_2$ layers are distorted significantly in the interfacial region compared with those away from the interface. The orientation of the organic moieties is different in these two heterostructures, and the C−H bonding angle remains nearly the same along c direction in α-CH$_3$NH$_3$SnI$_3$/TiO$_2$ while changes slightly in β-CH$_3$NH$_3$PbI$_3$/TiO$_2$.

3.2. Electrostatic Potential and Carrier Separation in Perovskite-Based Heterostructures. To study separation of electron and hole pairs in the heterostructures, we calculate the potential drop across the heterojunctions. The artificial potential in the vacuum has been compensated by introducing a dipole layer as done in our previous studies.[40,41]

$$V_{com}(\mathbf{r}) = 4\pi m(\mathbf{r}/r_m - 1/2), \qquad 0 < \mathbf{r} < r_m \qquad (5)$$

where m is the surface dipole density of the slab, r_m is the periodic length in the direction perpendicular to the slab.

We only report the calculations of CH$_3$NH$_3$Sn$_{0.50}$Pb$_{0.50}$I$_3$/TiO$_2$ for mixed Pb-Sn heterostructures to simplify the analysis. The potential across the three heterostructures with different Pb/Sn ratio is shown in Figure 4. It is worth mentioning that the potential drop along the perovskites side in CH$_3$NH$_3$PbI$_3$/TiO$_2$ is notably steeper than that in CH$_3$NH$_3$SnI$_3$/TiO$_2$ and CH$_3$NH$_3$Sn$_{0.50}$Pb$_{0.50}$I$_3$/TiO$_2$, indicating that the Pb-rich heterostructures are efficient in separating the photogenerated carriers. Because the potential drop is close to the interface, a large amount of electrons can be accumulated to the TiO$_2$ side. We have relaxed the pure halide materials and computed the ferroelectric polarization along the [0 0 1] direction. The polarization is very small and around the value of 1 μC/cm^2, indicating the built-in field in pure halide perovskites, as well as the potential drop, is very small. Actually, the polarization in the halide materials is attributed to the displacement of Pb(Sn) and the orientation of organic moieties(CH$_3$NH$_3$). The random orientation of organic moieties would lead to the decrease of the polarization and thus the electric field across the halide perovskites along [0 0 1] direction. Therefore, the electric field across the heterostructures is caused by the interfacial interactions in CH$_3$NH$_3$PbI$_3$/TiO$_2$.

Computed density of states (DOS) and partial density of states (PDOS) of the Pb-Sn mixed heterostructures are shown in Figure 5. The band alignment for TiO$_2$ and CH$_3$NH$_3$PbI$_3$ is shown in Figure 5(d). It can be seen that the Ti-3d states in the vicinity of the Fermi level result in the charge accumulation at interface, rendering TiO$_2$ an excellent ETM. The Pb-6p states in the CBM are much weaker compared with the pure halide perovskites, implying electron transfer between Pb-6p and Ti-3d states. Computed DOS and PDOS for relaxed TiO$_2$ and stand-alone TiO$_2$ and CH$_3$NH$_3$Sn$_x$Pb$_{1-x}$I$_3$ (x = 0, 0.5, 1), whose lattice constants and atomic positions are taken directly from the optimized heterogeneous structures, are given in Figures S1−S9.
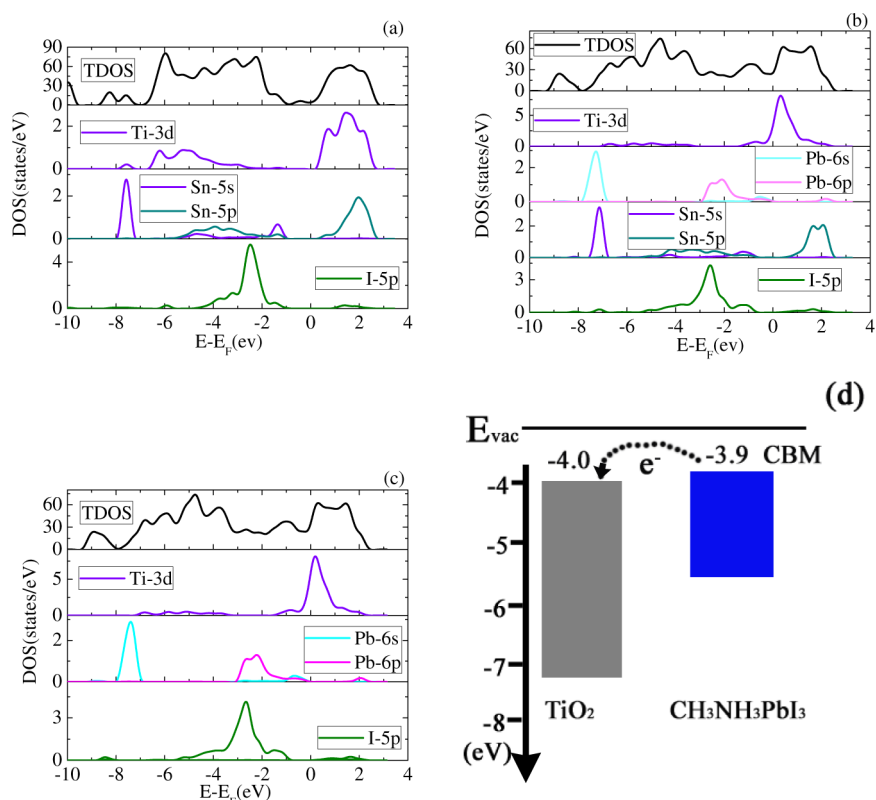
Figure 5. Computed DOS and PDOS for (a) $CH_3NH_3SnI_3/TiO_2$, (b) $CH_3NH_3Sn_{0.50}Pb_{0.50}I_3/TiO_2$, and (c) $CH_3NH_3PbI_3/TiO_2$ heterostructures, respectively. (d) Band alignment for TiO_2 and $CH_3NH_3PbI_3$. The shaded areas indicate the band gaps with the CBM on top. In (a)-(c), the Fermi level is set to zero. Computed Ti-3d states for the TiO_2 part, whose lattice constants and atomic positions are taken directly from the optimized heterogeneous structures, are displayed in Figure S3. Computed DOS and PDOS for the stand-alone $CH_3NH_3Sn_xPb_{1-x}I_3$ with x corresponding to 1, 0.50, and 0, whose lattice constants and atomic positions are taken directly from the optimized heterogeneous structures, are given in Figures S5, S7, and S9, respectively. It can be seen that the charge accumulation is entirely due to the interface of heterogeneous structures.

The electrons are transferred from $CH_3NH_3PbI_3$ to TiO_2 due to the CBM of TiO_2 having lower energy compared to the CBM of $CH_3NH_3PbI_3$. These electrons render interfacial Ti-3d states metallic, and hence the DOS in Figure 5(b) and (c) is non-zero at the Fermi energy for these states. However, away from the interface, we expect that both $CH_3NH_3PbI_3$ and TiO_2 become insulating as in bulk (see Figures S3 and S9). The interfacial electrons are then transported via bulk TiO_2, and the holes left behind in the interfacial PbI_2 layer are transported via bulk $CH_3NH_3PbI_3$ due to the electric field present in the structure (Figure 4). It is interesting that the Ti-3d states are shifted toward the CBM so that the charge accumulation from TiO_2 side disappears in $CH_3NH_3SnI_3/TiO_2$ (see Figure 5(a)), indicating that the electron hopping between Sn-5p and Ti-3d states is largely prohibited in the Sn-rich halide perovskite heterostructures. Meanwhile, Sn-5p states remain unchanged compared with pure $CH_3NH_3SnI_3$, and this can partly explain why the potential drop is relatively smaller in the Sn-rich heterostructures. These results provide a clear explanation that the $CH_3NH_3PbI_3/TiO_2$ planar solar cell is highly effective in charge carrier separation with high photovoltaic performance.

The electron localization in the orbital ϕ can be described by the electron localization function (ELF) as[42]

$$ELF = \frac{1}{1 + \left(\dfrac{D_\delta(x,y,z)}{D_{\delta,0}(x,y,z)}\right)^2} \qquad (6)$$

where

$$D_\delta(x, y, z) = \frac{1}{2}\sum_{j=1}^{N}|\Delta\phi|^2 - \frac{1}{8}\frac{|\Delta\rho|^2}{\rho} \qquad (7)$$

and

$$D_{\delta,0}(x, y, z) = \frac{3}{10}(3\pi^2)^{2/3}\rho^{5/3} \qquad (8)$$

Here, $D_\delta(x,y,z)$ is the leading term of the Taylor expansion of the spherically averaged δ-spin pair probability, and $D_{\delta,0}(x,y,z)$ is the corresponding value for the homogeneous electron gas. The ELF of these three heterostructures is shown in Figure 6. The ELF in the $CH_3NH_3PbI_3$ side of the Pb-rich heterostructure is relatively lower compared with the Sn-rich heterostructure, and this is caused by the electron transfer in the interface. Moreover, an abrupt change of ELF near the interface can be seen clearly. The lower ELF in the perovskite side further leads to carrier transfer and electron and hole separation. The electron hopping between the Pb(Sn) and Ti-3d states can be tuned by the Pb/Sn ratio. The higher the Pb/Sn ratio, the more significant the carrier transport across the interface and the stronger the separation of electron and hole pairs in the heterostructures. We will discuss the effect on the electronic and optical properties caused by the Pb/Sn ratio in more detail below.

3.3. Effect of Pb/Sn Ratio on Optical Absorption. The Liouville equation within TD-DFT can be written as[22]
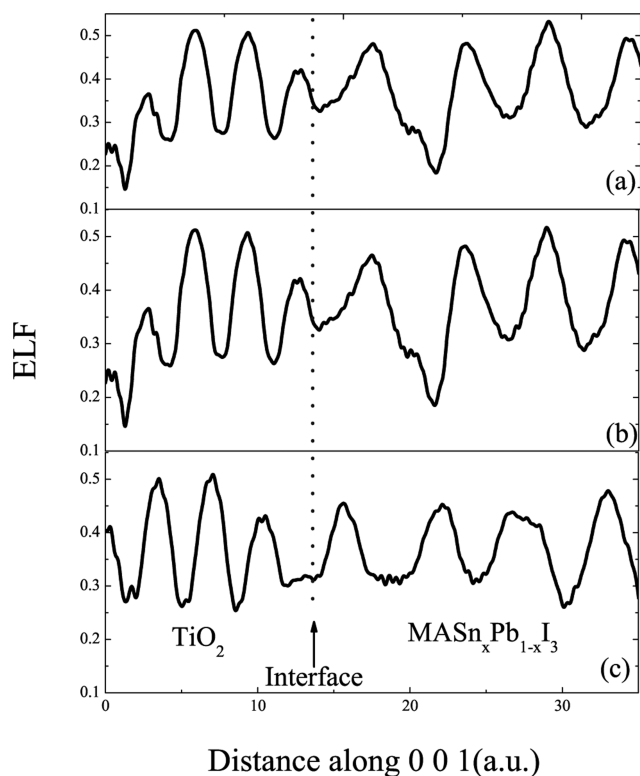
Figure 6. Distribution of ELF across the (a) CH$_3$NH$_3$SnI$_3$/TiO$_2$, (b) CH$_3$NH$_3$Sn$_{0.50}$Pb$_{0.50}$I$_3$/TiO$_2$, and (c) CH$_3$NH$_3$PbI$_3$/TiO$_2$ heterostructures averaged over the plane parallel to the film.
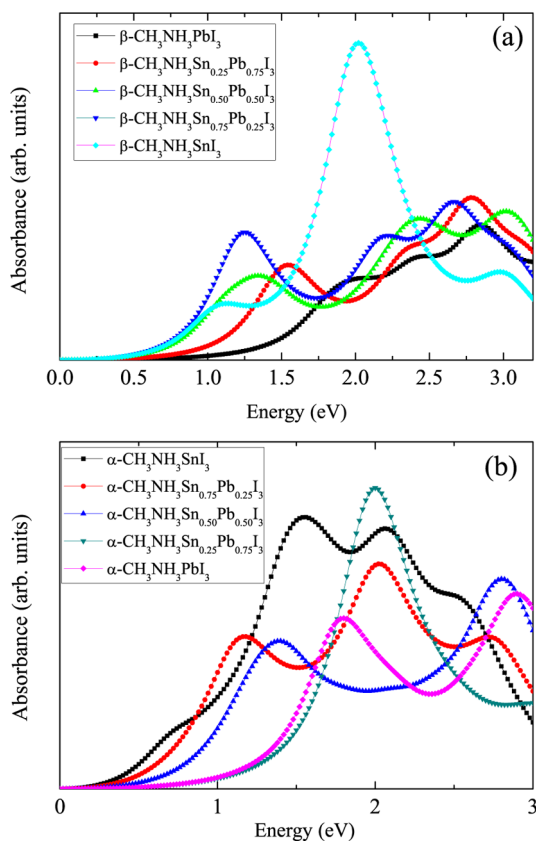
Figure 7. Absorbance for (a) β-CH$_3$NH$_3$Sn$_x$Pb$_{1-x}$I$_3$ and (b) α-CH$_3$NH$_3$Sn$_x$Pb$_{1-x}$I$_3$ calculated from the TD-DFT.

Table 3. Total Energies of the α and β Phases Per Formula Unit (fu) and Their Difference for Different Concentrations (x) of Sn

x	E$_\alpha$(Ry)	E$_\beta$(Ry)	E$_\alpha$-E$_\beta$(Ry)
0	−2031.3516	−2031.3548	0.0031
0.25	−1925.6287	−1925.6285	−0.0002
0.5	−1819.9028	−1819.9021	−0.0007
0.75	−1714.1813	−1714.1801	−0.0012
1	−1608.4579	−1608.4560	−0.0019

Table 4. Band gaps of the Mixed Pb-Sn Compounds and Heterostructures Calculated by DFT, TD-DFT, and SOC-GW[23] As Well As the Experimental Values (units in eV)[8]

	DFT	TD-DFT	SOC-GW	exp.
α-CH$_3$NH$_3$SnI$_3$	0.48	0.60	—	0.90
α-CH$_3$NH$_3$Sn$_{0.75}$Pb$_{0.25}$I$_3$	0.73	0.90	—	1.13
α-CH$_3$NH$_3$Sn$_{0.50}$Pb$_{0.50}$I$_3$	1.01	1.10	—	1.17
α-CH$_3$NH$_3$Sn$_{0.25}$Pb$_{0.75}$I$_3$	1.32	1.42	—	—
α-CH$_3$NH$_3$PbI$_3$	1.20	1.30	—	—
β-CH$_3$NH$_3$SnI$_3$	0.52	0.85	1.31	—
β-CH$_3$NH$_3$Sn$_{0.75}$Pb$_{0.25}$I$_3$	0.64	0.75	1.20	—
β-CH$_3$NH$_3$Sn$_{0.50}$Pb$_{0.50}$I$_3$	0.88	0.80	1.41	—
β-CH$_3$NH$_3$Sn$_{0.25}$Pb$_{0.75}$I$_3$	1.03	1.20	1.37	1.19
β-CH$_3$NH$_3$PbI$_3$	1.30	1.50	1.64	1.53

$$i\frac{d\rho'(t)}{dt} = \pounds \cdot \rho'(t) + [V'_{ext}(t), \rho^0] \qquad (9)$$

where $\rho(t)$ is the one-electron Kohn-Sham density matrix, ρ^0 is the unperturbed density matrix, $\rho'(t) = \rho(t) - \rho^0$, and $V'_{ext}(t)$ denotes the external perturbation. With Fourier transformation, eq 9 becomes

$$(\omega - \pounds) \cdot \tilde{\rho}'(\omega) = [\tilde{V}'_{ext}(\omega), \rho^0] \qquad (10)$$

in the frequency domain.

The optical absorption curves for β and α phase perovskites with different Pb/Sn ratio are shown in Figure 7. For the β-CH$_3$NH$_3$Sn$_x$Pb$_{1-x}$I$_3$, the onset of absorption is increased with increasing of Pb/Sn ratio for $x < 0.5$. It is interesting that the absorption edge does not change obviously for $x \geq 0.5$. The absorption spectra for β-CH$_3$NH$_3$PbI$_3$ and β-CH$_3$NH$_3$Sn$_{0.25}$Pb$_{0.75}$I$_3$ agree well with the experiments.[6−8] However, the spectra for β-CH$_3$NH$_3$Sn$_{0.50}$Pb$_{0.50}$I$_3$, β-CH$_3$NH$_3$Sn$_{0.75}$Pb$_{0.25}$I$_3$, and β-CH$_3$NH$_3$SnI$_3$ are inconsistent with experiments, indicating that the β phase with $I4cm$ symmetry is not the case for Sn-rich halide perovskite. Indeed, experimental measurements show that the Sn-rich halide perovskites are in α phase with $P4mm$ symmetry.[6,7] To further clarify this point, we compute the absorption curves for the Sn-rich α phase perovskites, and the results are given in Figure 7. For α phase, the absorption edge monotonically decreases as the Sn concentration is lowered for $x \geq 0.5$. The absorption edge is nonlinear and consistent with the experiments shown in Figure S10 with $x < 0.5$, indicating α phase is not the structure for Pb-rich halide perovskites. Combined with β phase in Pb-rich perovskites, the optical absorption of the α phase in Sn-rich compounds agrees well with the experimental results shown in Figure S11. Therefore, we conclude that both the α phase in Sn-rich compounds and β phase in Pb-rich perovskites should be considered in order to compare with the experiments.

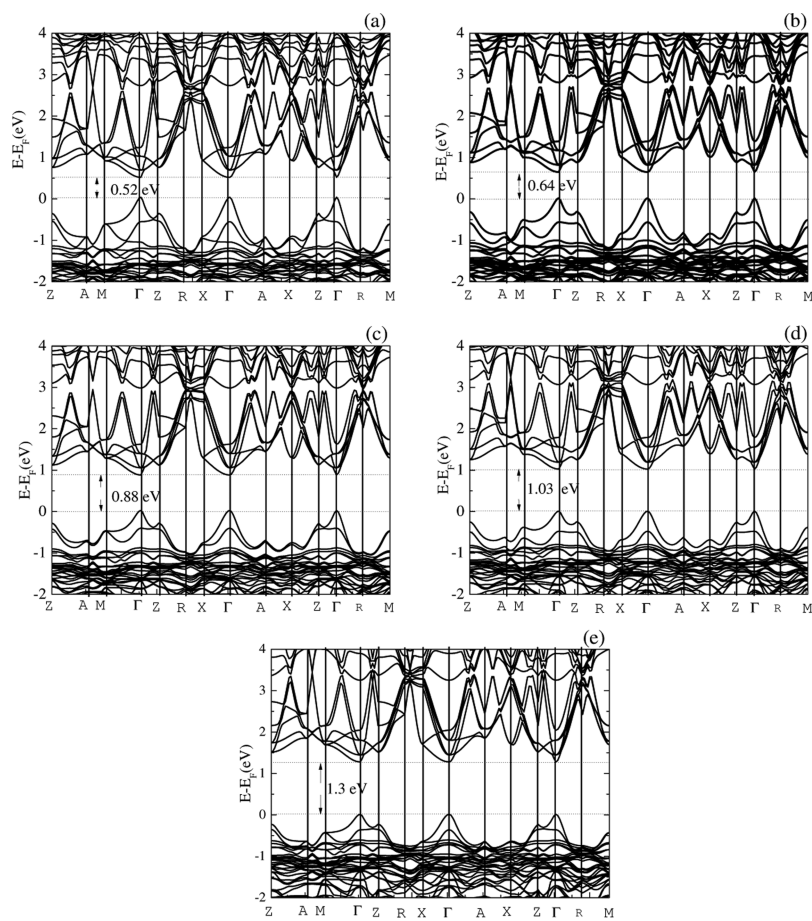The stability of the α phase increases when Sn concentration increases. This is seen from Table 3, where we show the

Figure 8. Band structure for β-CH$_3$NH$_3$Sn$_x$Pb$_{1-x}$I$_3$ with x = (a) 1, (b) 0.75, (c) 0.50, (d) 0.25, and (e) 0, respectively. The Fermi level is set to zero.
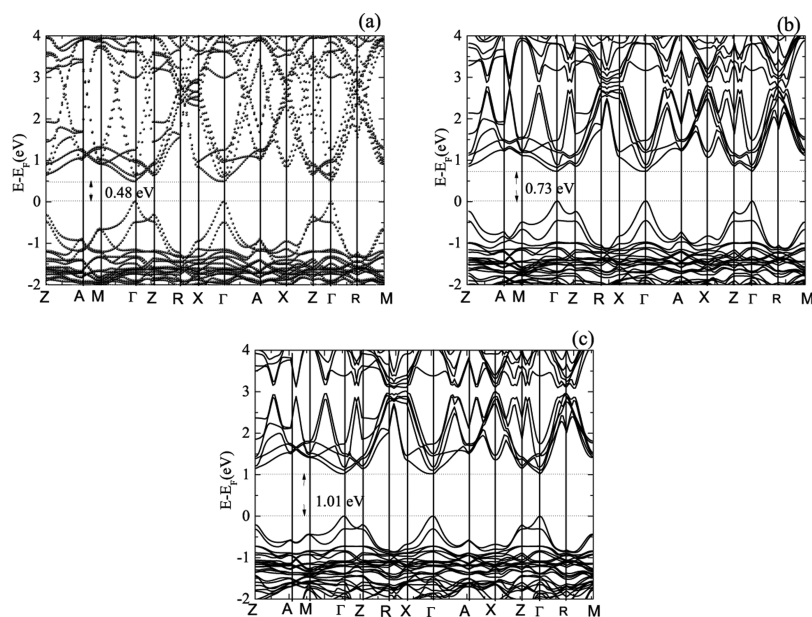

Figure 9. Band structure for α-CH$_3$NH$_3$Sn$_x$Pb$_{1-x}$I$_3$ with x = (a) 1, (b) 0.75, and (c) 0.50, respectively. The Fermi level is set to zero.

total energies of the α and β phases per formula unit and their difference for different concentrations (x) of Sn. As is evident from Table 3, the α phase becomes more stable when $x \geq 0.5$. We note that for $x = 0.25$ the energy difference between α and β phases is within the accuracy of our computation ($\sim$0.2 mRy/fu).

The stability of the undistorted α phase over distorted β phase can be understood in terms of the geometric tolerance factor t, defined as $(R_{MA} + R_I)/\sqrt{2}\,(R_{Pb/Sn} + R_I)$. Due to a smaller ionic radius for Sn^{2+} (R_{Sn} = 0.93 Å) compared to that for Pb^{2+} (R_{Pb} = 1.19 Å) the tolerance factor is 0.92 for CH$_3$NH$_3$SnI$_3$, whereas it is 0.85 for CH$_3$NH$_3$PbI$_3$.[43] Therefore, the more Sn that is
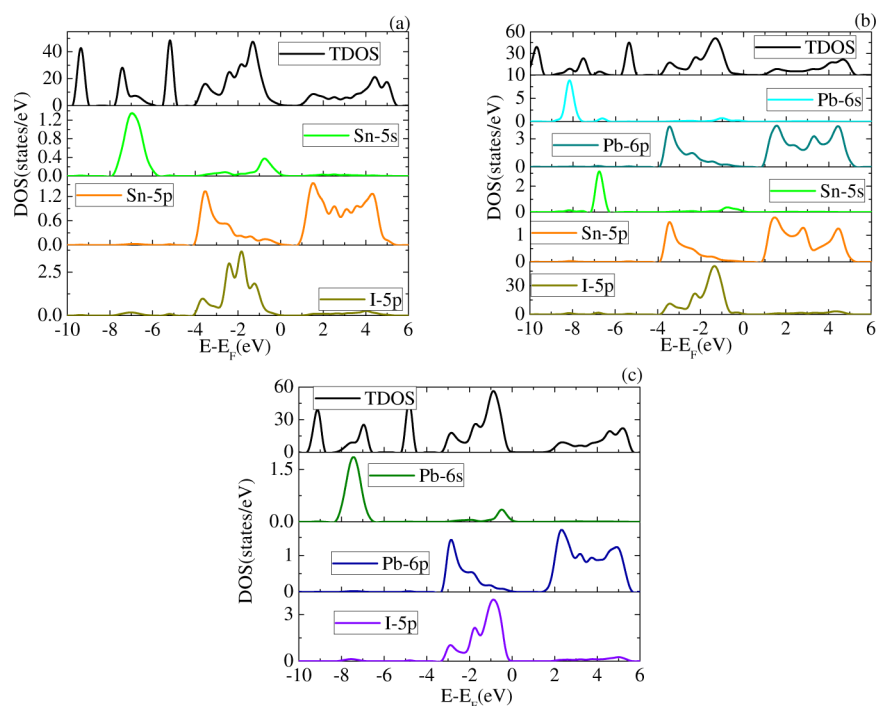
Figure 10. Computed DOS and PDOS for (a) α-CH$_3$NH$_3$SnI$_3$, (b) β-CH$_3$NH$_3$Sn$_{0.25}$Pb$_{0.75}$I$_3$, and (c) β-CH$_3$NH$_3$PbI$_3$, respectively. The Fermi level is set to zero.
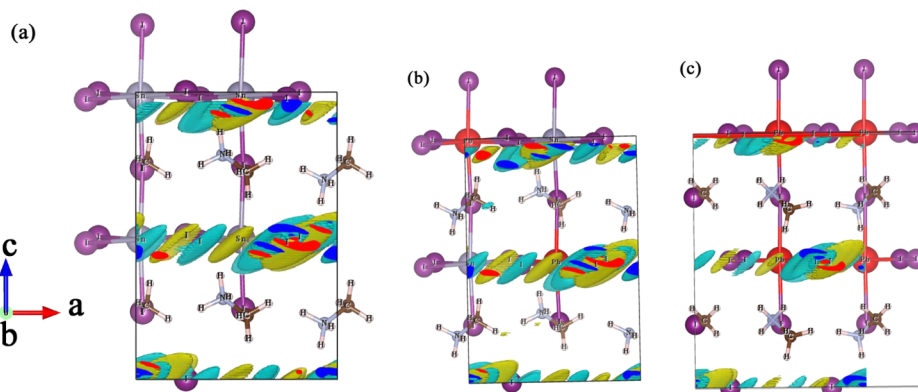
Figure 11. Response charge distribution for (a) α-CH$_3$NH$_3$SnI$_3$, (b) α-CH$_3$NH$_3$Sn$_{0.50}$Pb$_{0.50}$I$_3$, and (c) β-CH$_3$NH$_3$PbI$_3$, respectively. The gray and red balls indicate the Sn and Pb atoms, respectively.

Table 5. Calculated Polarization (P) for α and β Phase Pb-Sn Halide Perovskites

	polarization (μC/cm^2)
α-CH$_3$NH$_3$SnI$_3$	0.97
α-CH$_3$NH$_3$Sn$_{0.75}$Pb$_{0.25}$I$_3$	0.95
α-CH$_3$NH$_3$Sn$_{0.50}$Pb$_{0.50}$I$_3$	0.74
α-CH$_3$NH$_3$Sn$_{0.25}$Pb$_{0.75}$I$_3$	0.64
α-CH$_3$NH$_3$PbI$_3$	0.56
β-CH$_3$NH$_3$SnI$_3$	0.98
β-CH$_3$NH$_3$Sn$_{0.75}$Pb$_{0.25}$I$_3$	0.99
β-CH$_3$NH$_3$Sn$_{0.50}$Pb$_{0.50}$I$_3$	1.00
β-CH$_3$NH$_3$Sn$_{0.25}$Pb$_{0.75}$I$_3$	1.00
β-CH$_3$NH$_3$PbI$_3$	0.98

introduced in the system, the higher the tolerance factor is and thus likelihood of the appearance of the α phase.

Additionally, we found that the Sn−I bond length is shorter than that of Pb−I, thereby effectively reducing the volume of

the octahedral cage. It is known that when the ratio of volume of A centered-polyhedra to the volume of B centered-octahedra increases, the undistorted phase is favored in perovskite oxides.[44] Here, when the concentration of Sn increases, effectively the volume ratio of CH$_3$NH$_3$-centered polyhedra to Pb(Sn)-centered octahedra increases, thereby favoring the undistorted α phase. For simplicity, we only provide computation results for α phase of CH$_3$NH$_3$SnI$_3$, CH$_3$NH$_3$Sn$_{0.75}$Pb$_{0.25}$I$_3$, and CH$_3$NH$_3$Sn$_{0.50}$Pb$_{0.50}$I$_3$ and β phase of CH$_3$NH$_3$PbI$_3$ and CH$_3$NH$_3$Sn$_{0.25}$Pb$_{0.75}$I$_3$ below.

The band structures for β and α phase perovskites with different Pb/Sn ratio are shown in Figure 8 and 9, respectively. The band gap of β phase increases monotonically with the increase of Pb concentration. The higher the Pb/Sn ratio, the wider band gap is. The blue shift of absorption with increasing the Pb/Sn ratio agrees well with the DFT calculations reported recently.[23] However, the linear relationship between Pb/Sn ratio and band gap in β or α phase is inconsistent with the

experiments. Here, our TD-DFT calculations predict that the structures are in good agreement with the experiments where β phase exists in Pb-rich perovskites and α phase in Sn-rich perovskites.[7] So, TD-DFT predicts results more consistent with experiments than DFT for the mixed Pb-Sn organohalide perovskites.

The degeneracy and the symmetry of the CBM and VBM do not change significantly with increasing the Pb/Sn ratio. As far as $CH_3NH_3Sn_{0.25}Pb_{0.75}I_3$ is concerned, the VBM of the I-5p and Sn-5p states do not shift with respect to the Fermi level as a small amount of DOS can still be identified close to the Fermi level (the corresponding DOS and PDOS are shown in Figure 10). The shift of I-5p states in the vicinity of VBM is mainly caused by the competition between the Sn-5s and Pb-6s states in the similar energy region, and the slight change of Pb-6s states can be observed in the PDOS. Therefore, the band gap can be tuned by the addition of Sn in the $MAPbI_3$ without changing the symmetry in the vicinity of CBM and VBM. The shift of the I-5p states near the VBM may have some effect on the optical transition states and optical absorption. The band gaps of the mixed perovskites with different Pb/Sn ratio in both β and α phases are given in Table 4. One can see that the TD-DFT results agree well with the experiments. Although DFT calculations give a linear relation between the Pb/Sn ratio and the band gap for the mixed compounds in β or α phase, the results are inconsistent with the experiments. The α phase must be considered in Sn-rich compounds, while the β phase is considered in Pb-rich perovskites for computing their properties.[7]

3.4. Response Charge and Ferroelectric Properties.
The response charge density to a perturbation within standard batch representation is given by[22]

$$n'(\mathbf{r}) = 2 \sum_{v} \phi_v^0(\mathbf{r}) q_v(\mathbf{r}) \tag{11}$$

where $\phi_v^0(\mathbf{r})$ are ground-state eigenfunctions of the unperturbed Kohn−Sham Hamiltonian, $q_v(\mathbf{r})$ defines the standard batch representation of the density-matrix response.

The response charge density for $CH_3NH_3SnI_3$, $CH_3NH_3Sn_{0.50}Pb_{0.50}I_3$, and $CH_3NH_3PbI_3$ is shown in Figure 11. It is clear that the charge density is mainly occupied in the $Pb(Sn)I_2$ layers, while nearly no charge density can be observed in the organic layers, implying that the ferroelectric polarization mainly originates from the inorganic layers. The response charge density is associated significantly with the Pb-6s and Sn-5s states which are the origin of the stereochemical activity of the lone pair. Moreover, the charge density is not influenced dramatically by the Pb/Sn ratio, implying that the ferroelectricity does not change significantly in the mixed organometal halide perovskites.

The calculated polarization is given in Table 5. Both α and β phase organometal halide perovskites have a relatively small polarization compared with the classic ferroelectrics. Polarization decreases slightly with increasing of Pb concentration, indicating Pb may stabilize the structure. The displacements between the positive and negative ions in $Pb(Sn)I_2$ layers are small, resulting in a smaller polarization. Moreover, the organic moieties contribute slightly to the ferroelectric polarization due to the random orientation of the C−N bonding. $Pb(Sn)-I_6$ cages only distort within ab plane in the β phase structure and do not make a significant contribution to the ferroelectricity along the c direction. An enhanced polarization is expected if the C−N bonding is arranged along the specific direction under external stimuli.

4. CONCLUSION
Both TD-DFT and DFT calculations have been performed to investigate the separation of charge carriers in CH_3NH_3-$Sn_xPb_{1-x}I_3/TiO_2$ heterostructures. Pb-rich perovskites-based heterostructures can produce a sharp potential drop across the interface and result in stronger separation of electrons and holes pairs. The potential wells in the heterostructures are caused by the charge accumulation in the TiO_2 side. Our computation results offer an answer to the question why the Pb-rich perovskites exhibit much higher power conversion efficiencies than the Sn-rich counterparts for solar-cell applications. Moreover, TD-DFT calculations predict a better tendency of bandgap tuning with varying Pb/Sn ratio and optical absorption in agreement with experimental results. The distribution of response charge density suggests that the ferroelectric polarization of the organometal halide perovskites is mainly originated from the contribution of the $Pb(Sn)I_2$ layers. The relative displacements in the inorganic layers are much smaller so that trivial ferroelectricity can be observed in the organometal halide perovskites.

■ ASSOCIATED CONTENT
Ⓢ Supporting Information
PDOS of TiO_2 and $CH_3NH_3Sn_xPb_{1-x}I_3$ taken from the $CH_3NH_3Sn_xPb_{1-x}I_3/TiO_2$ heterostructures; experimental optical spectra for $CH_3NH_3Sn_xPb_{1-x}I_3$. The Supporting Information is available free of charge on the ACS Publications website at DOI: 10.1021/jacs.5b04015.

■ AUTHOR INFORMATION
Corresponding Authors
*hjfeng@nwu.edu.cn
*xzeng1@unl.edu
Notes
The authors declare no competing financial interest.

■ ACKNOWLEDGMENTS

■ REFERENCES
(1) Kojima, A.; Teshima, K.; Shirai, Y.; Miyasaka, T. *J. Am. Chem. Soc.* **2009**, *131*, 6050−6051.
(2) *National Center for Photovoltaics* http://www.nrel.gov/ncpv.
(3) Zhou, H.; Chen, Q.; Li, G.; Luo, S.; Song, T.-b.; Duan, H.-S.; Hong, Z.; You, J.; Liu, Y.; Yang, Y. *Science* **2014**, *345*, 542−546.

(4) Noel, N. K.; Stranks, S. D.; Abate, A.; Wehrenfennig, C.; Guarnera, S.; Haghighirad, A. A.; Sadhanala, A.; Eperon, G. E.; Johnston, M. B.; Petrozza, A. M.; Herz, L. M.; Snaith, H. J. *Energy Environ. Sci.* **2014**, *7*, 3061−3068.

(5) Hao, F.; Stoumpos, C. C.; Cao, D. H.; Chang, R. P. H.; Kanatzidis, M. G. *Nat. Photonics* **2014**, *8*, 489−494.

(6) Stoumpos, C. C.; Malliakas, C. D.; Kanatzidis, M. G. *Inorg. Chem.* **2013**, *52*, 9019−9038.

(7) Hao, F.; Stoumpos, C. C.; Chang, R. P. H.; Kanatzidis, M. G. *J. Am. Chem. Soc.* **2014**, *136*, 8094−8099.

(8) Ogomi, Y.; Morita, A.; Tsukamoto, S.; Saitho, T.; Fujikawa, N.; Shen, Q.; Toyoda, T.; Yoshino, K.; Pandey, S. S.; Ma, T.; Hayase, S. *J. Phys. Chem. Lett.* **2014**, *5*, 1004−1011.

(9) Chiarella, F.; Zappettini, A.; Licci, F. *Phys. Rev. B: Condens. Matter Mater. Phys.* **2008**, *77*, 045129.

(10) Umebayashi, T.; Asai, K.; Kondo, T.; Nakao, A. *Phys. Rev. B: Condens. Matter Mater. Phys.* **2003**, *67*, 155405.

(11) Mosconi, E.; Amat, A.; Nazeeruddin, M. K.; Gratzel, M.; de Angelis, F. *J. Phys. Chem. C* **2013**, *117*, 13902−13913.

(12) Feng, J.; Xiao, B. *J. Phys. Chem. Lett.* **2014**, *5*, 1278−1282.

(13) Amat, A.; Mosconi, E.; Ronca, E.; Quarti, C.; Umari, P.; Nazeeruddin, M. K.; Gratzel, M.; Angelis, F. D. *Nano Lett.* **2014**, *14*, 3608−3616.

(14) Even, J.; Pedesseau, L.; Jancu, J.; Katan, C. *J. Phys. Chem. Lett.* **2013**, *4*, 2999−3005.

(15) Even, J.; Pedesseau, L.; Jancu, J.; Katan, C. *Phys. Status Solidi RRL* **2014**, *8*, 31−35.

(16) Giorgi, G.; Fujisawa, J.-I.; Segawa, H.; Yamashita, K. *J. Phys. Chem. Lett.* **2013**, *4*, 4213−4215.

(17) Yin, W.-J.; Yang, J.-H.; Kang, J.; Yan, Y.; Wei, S.-H. *J. Mater. Chem. A* **2015**, *3*, 8926−8942.

(18) Feng, J.; Xiao, B. *J. Phys. Chem. C* **2014**, *118*, 19655−19660.

(19) Zhu, X.; Su, H.; Marcus, R. A.; Michel-Beyerle, M. E. *J. Phys. Chem. Lett.* **2014**, *5*, 3061−3065.

(20) Brivio, F.; Butler, K. T.; Walsh, A.; Schilfgaarde, M. V. *Phys. Rev. B: Condens. Matter Mater. Phys.* **2014**, *89*, 155204.

(21) Walker, B.; Saitta, A. M.; Gebauer, R.; Baroni, S. *Phys. Rev. Lett.* **2006**, *96*, 113001.

(22) Rocca, D.; Gebauer, R.; Saad, Y.; Baroni, S. *J. Chem. Phys.* **2008**, *128*, 154105.

(23) Mosconi, E.; Umari, P.; Angelis, F. D. *J. Mater. Chem. A* **2015**, *3*, 9208−9215.

(24) Burschka, J.; Pellet, N.; Moon, S.; Humphry-Baker, R.; Gao, P.; Nazeeruddin, M. K.; Gratzel, M. *Nature* **2013**, *499*, 316−319.

(25) Zhou, H.; Chen, Q.; Li, G.; Luo, S.; Song, T.-b.; Duan, H.-S.; Hong, Z.; You, J.; Liu, Y.; Yang, Y. *Science* **2014**, *345*, 542−546.

(26) McGehee, M. D. *Nat. Mater.* **2014**, *13*, 845−846.

(27) Im, J.-H.; Jang, I.-H.; Pellet, N.; Gratzel, M.; Park, N.-G. *Nat. Nanotechnol.* **2014**, *9*, 927−932.

(28) Gratzel, M. *Nat. Mater.* **2014**, *13*, 838−842.

(29) Lee, M. M.; Teuscher, J.; Miyasaka, T.; Murakami, T. N.; Snaith, H. J. *Science* **2012**, *338*, 643−647.

(30) Etgar, L.; Gao, P.; Xue, Z.; Peng, Q.; Chandiran, A. K.; Liu, B.; Nazeeruddin, Md. K.; Gratzel, M. *J. Am. Chem. Soc.* **2012**, *134*, 17396−17399.

(31) Mei, A.; Li, X.; Liu, L.; Ku, Z.; Liu, T.; Rong, Y.; Xu, M.; Hu, M.; Chen, J.; Yang, Y.; Gratzel, M.; Han, H. *Science* **2014**, *345*, 295−298.

(32) (a) Feng, H.-J.; Wang, M.; Liu, F.; Duan, B.; Tian, J.; Guo, X. *J. Alloys Compd.* **2015**, *628*, 311−316. (b) Feng, H.-J. *Mater. Chem. Phys.* **2015**, *153*, 405−409.

(33) (a) Mosconi, E.; Ronca, E.; De Angelis, F. *J. Phys. Chem. Lett.* **2014**, *5*, 2619−2625. (b) Roiati, V.; Mosconi, E.; Listorti, A.; Colella, S., II; Gigli, G.; De Angelis, F. *Nano Lett.* **2014**, *14*, 2168−2174.

(34) Giannozzi, P.; Baroni, S.; Bonini, N.; Calandra, M.; Car, R.; Cavazzoni, C.; Ceresoli, D.; Guido, L. C.; Cococcioni, M.; Dabo, I.; Corso, A. D.; Fabris, S.; Fratesi, G.; de Gironcoli, S.; Gebauer, R.; Gerstmann, U.; Gougoussis, C.; Kokalj, A.; Lazzeri, M.; Martin-Samos, L.; Marzari, N.; Mauri, F.; Mazzarello, R.; Paolini, S.; Pasquarello, A.; Paulatto, L.; Sbraccia, C.; Scandolo, S.; Sclauzero, G.; Seitsonen, A. P.; Smogunov, A.; Umari, P.; Wentzcovitch, R. M. *J.Phys.: Condens. Matter* **2009**, *21*, 395502.

(35) Perdew, J. P.; Ruzsinszky, A.; Csonka, G. I.; Vydrov, O. A.; Scuseria, G. E.; Constantin, L. A.; Zhou, X.; Burke, K. *Phys. Rev. Lett.* **2008**, *100*, 136406.

(36) Blöchl, P. E. *Phys. Rev. B: Condens. Matter Mater. Phys.* **1994**, *50*, 17953.

(37) Corso, A. D. *Comput. Mater. Sci.* **2014**, *95*, 337−350.

(38) King-Smith, R. D.; Vanderbilt, D. *Phys. Rev. B: Condens. Matter Mater. Phys.* **1993**, *47*, 1651(R).

(39) Vanderbilt, D.; King-Smith, R. D. *Phys. Rev. B: Condens. Matter Mater. Phys.* **1993**, *48*, 4442.

(40) Feng, H.-J. *Europhys. Lett.* **2013**, *101*, 67007.

(41) Feng, H.-J. *J. Appl. Phys.* **2013**, *114*, 123916.

(42) Becke, A. D.; Edgecombe, K. E. *J. Chem. Phys.* **1990**, *92*, 5397.

(43) Chilvery, A. K.; Batra, A. K.; Yang, B.; Xiao, K.; Guggilla, P.; Aggarwal, M. D.; Surabhi, R.; Lal, R. B.; Currie, J. R.; Penn, B. G. *J. Photonics for Energy* **2015**, *5*, 057402.

(44) Magyari-Kope, B.; Vitos, L.; Johansson, B.; Kollar, J. *Phys. Rev. B: Condens. Matter Mater. Phys.* **2002**, *66*, 092103.